frontiers in Chemistry

ORIGINAL RESEARCH
published: 14 October 2021
doi: 10.3389/fchem.2021.746031

Fabrication of g-C_3N_4 Nanosheets Anchored With Controllable CdS Nanoparticles for Enhanced Visible-Light Photocatalytic Performance

Minggui Wang[1,2], *Min Wang*[1], *Fang Peng*[1], *Xiaohuan Sun*[2] *and Jie Han*[2]*

[1]Guangling College, Yangzhou University, Yangzhou, China, [2]School of Chemistry and Chemical Engineering, Yangzhou University, Yangzhou, China

Herein, g-C_3N_4/CdS hybrids with controllable CdS nanoparticles anchoring on g-C_3N_4 nanosheets were constructed. The effects of CdS nanoparticles on photocatalytic H_2 production and organic molecule degradation for g-C_3N_4/CdS hybrids were investigated. The maximum rate of H_2 production for g-C_3N_4/CdS sample was 1,070.9 μmol g^{-1} h^{-1}, which was about four times higher than that of the individual g-C_3N_4 nanosheet sample. The enhanced photocatalytic performance for prepared hybrids could be mainly attributed to the following causes: the formed heterojunctions can contribute to the light absorption and separation of photogenerated electrons and holes, the two-dimensional layered structure facilitates the transmission and transfer of electrons, and high specific surface area could provide more exposed active sites.

Keywords: G-C3N4, CdS, hybrids, photocatalyst, visible light

OPEN ACCESS

Edited by:
Wee-Jun Ong,
Xiamen University Malaysia, Malaysia

Reviewed by:
Lutfi Kurnianditia Putri,
Universiti Sains Malaysia (USM), Malaysia
Li Yuhan,
Chongqing Technology and Business University, China

***Correspondence:**
Jie Han
hanjie@yzu.edu.cn

Specialty section:
This article was submitted to Catalysis and Photocatalysis, a section of the journal Frontiers in Chemistry

Received: *23 July 2021*
Accepted: *02 September 2021*
Published: *14 October 2021*

Citation:
Wang M, Wang M, Peng F, Sun X and Han J (2021) Fabrication of g-C_3N_4 Nanosheets Anchored With Controllable CdS Nanoparticles for Enhanced Visible-Light Photocatalytic Performance. Front. Chem. 9:746031. doi: 10.3389/fchem.2021.746031

INTRODUCTION

Semiconductor materials have received widespread attention as promising photocatalysts for clean energy production and environmental problems. (Tong et al., 2012; Chang et al., 2016; Yu et al., 2017; Qi et al., 2018; Cao et al., 2019; Ng et al., 2021). Recently, g-C_3N_4 has received considerable attention as a promising photocatalyst, owing to its ease of preparation, high stability, low cost, clean and low toxicity, narrowed bandgap (~2.7 eV), and special two-dimensional (2D) layered structure (Shi et al., 2016; Teng et al., 2017; Han et al., 2018; Deng et al., 2019; Ong et al., 2020; Vu et al., 2020; Yu et al., 2021); however, diverse drawbacks include poor efficiency of light utilization and low separation of photogenerated charges during the application, making g-C_3N_4 less attractive for photocatalyst construction. (Tahir et al., 2014; Liu et al., 2017; Al Marzouqi et al., 2019; Fu et al., 2019; Fan et al., 2020). In addition, bulk g-C_3N_4 with a low surface area and irregular morphology prepared through the conventional method leads to the low transfer rate of interfacial charge and poor photocatalytic activity (Teng et al., 2017; Niu et al., 2018).

For the sake of the improved photocatalytic performance of pure g-C_3N_4, many strategies have been made to develop cheaper and recyclable catalysts, such as nanostructure design (Sun et al., 2012; Bai et al., 2013; Tahir et al., 2014; Lin et al., 2016; Zhou et al., 2018; Yang et al., 2019), loading with noble metals (Zhang et al., 2016; Duan et al., 2019; Wan et al., 2020) or doping non-metal elements (Guo et al., 2017; Liu et al., 2018; Li et al., 2020), and heterojunction construction (Zhang et al., 2013; Shi et al., 2017; Ji et al., 2018). However, noble metals are rare and too

expensive, and their stability is also a big challenge. Doping of non-metal elements would need high temperature and produce many noxious and odorous gases. While nanostructure design usually requires multiple synthetic steps, and templates are also required for special structures. Therefore, the enhanced photocatalytic performance of g-C_3N_4–based catalysts is still in urgent demand. As for heterojunction construction, the combination of g-C_3N_4 with another semiconductor that has well-matched band structures can not only expand the light absorption into the wide absorption region but also be formed between the two components, which effectively guarantee the separation of rapid charges and transfer in the contacted interface. As a visible light–responsive photocatalyst, CdS has also drawn great attention, and successfully applied in the fields of environmental protection, hydrogen evolution, and selective organic synthesis (Liu et al., 2015; Ren et al., 2019; Ai et al., 2020). Coupling g-C_3N_4 with CdS could be a feasible route to improve the photocatalytic activity. In previous reports, Chen et al. reported the synthesis of g-C_3N_4/CdS composites with a tunable density of CdS nanodots adopting the *in situ* photochemical deposition method (Chen et al., 2019). Cui et al. synthesized C_3N_4/CdS composites through a one-step calcination process at high temperatures (Cui, 2015). C_3N_4–CdS heterostructures were constructed by a precipitation–deposition route (Fu et al., 2013). All the reported g-C_3N_4/CdS composites showed higher photocatalytic activity and stability than individual g-C_3N_4 and CdS, ascribing to the synergic effect between g-C_3N_4 and CdS, which can effectively promote the charge separation and transfer. Although numerous heterostructure photocatalysts have been designed, the remarkable improvement of the photocatalytic effect has not been obtained. It was probably caused by large bulk volume or unreasonable contacted interfaces among the two or more components in photocatalysts. It has been investigated that the photocatalytic activity could be influenced by the following factors, such as particle sizes, morphology and structures, and preparation methods (Chen et al., 2010). Therefore, in order to optimize the photocatalytic performances of g-C_3N_4/CdS hybrids, some important factors should be taken into account, such as effective contact between two components, well-controlled morphology structure and particle size, and sufficiently exposed reactive active sites. However, few works have been found using the chemical deposition of CdS nanoparticles with controllable intensity and particle size onto g-C_3N_4 nanosheets to construct heterojunctions.

Herein, we realize the construction of the highly efficient heterostructured photocatalyst for the photocatalytic hydrogen evolution and degradation of pollutant molecules, where CdS nanoparticles with controllable particle sizes are obtained to modify g-C_3N_4 nanosheets through a facile chemical deposition process. It is found that the controllable CdS particle size has a significant effect on morphology, specific surface area, light absorption, and photocatalytic activity for prepared hybrids. The hydrogen generation rate of g-C_3N_4/CdS hybrids could reach up to 1,070.9 $\mu mol\, g^{-1}\ h^{-1}$. The effects of CdS nanoparticles for the light absorption and photoinduced charge transport, and the enhanced photocatalytic activities were systematically discussed.

EXPERIMENTAL

Synthesis

First, g-C_3N_4 nanosheets were prepared according to the previous report (Fan et al., 2020). Briefly, the amount of urea was heated at 570°C under air for 3 h, and the yellow product was obtained for further use. Then 10.0 mg of g-C_3N_4 nanosheets were dispersed into 20.0 ml aqueous solution containing different amounts of $CdCl_2.2.5H_2O$ (with 7.50, 15.0, and 22.5 mg $CdCl_2.2.5H_2O$, respectively) by ultrasonication for 30 min. Then 0.25 ml $NH_3{\cdot}H_2O$ and 5.0 ml thioacetamide (TAA) solution (with 5.5 mg TAA) was added, followed by a water bath at 60°C for 3 h. The resultant products were washed with water and ethanol three times and collected by centrifugation, followed by drying at 60°C for 4 h. After that, the as-prepared products were annealed at 300°C for 2 h in the nitrogen atmosphere by a tubular furnace to improve the crystallinity CdS. The as-prepared g-C_3N_4/CdS hybrids were denoted as g-C_3N_4/CdS-1, g-C_3N_4/CdS-2, and g-C_3N_4/CdS-3, respectively.

Photocatalytic Activity Tests

Photocatalytic degradation of organic pollutes was carried out in a photoreactor system (Xujiang XPA-7) with 5.0 mg of samples dispersed in a 25-ml target molecule solution (2.0×10^{-5} M). After that, a 400 W metal halide lamp with a filter ($\lambda > 400$ nm) was irradiated to trigger the photocatalytic reaction. The concentration of the degraded solution was detected by a UV-vis spectrophotometer.

The photocatalytic H_2 production was measured in a closed quartz reaction system (300 W Xe lamp with a filter as the light source, $\lambda > 400$ nm) using triethanolamine as the sacrificial reagent. 100 ml solution (with 20% triethanolamine and dispersed 10.0 mg samples) was continuously stirred at a fixed speed. The amount of H_2 was determined by the online gas chromatography (CEAULIGHT, GC-7920). During the photocatalytic tests, a cooling system was used to maintain the temperature constant.

Characterization

TEM (JEOL, JEM-2100) and HRTEM (FEI, Tecnai G2 F30 S-Twin TEM) were measured for imaging. The phase composition was measured by the Bruker D8 ADVANCE X-ray diffractometer (XRD). BET-specific surface areas and pore structures were determined by a Beishide 3H-2000PS2 system. XPS measurement was performed on a Thermo Scientific ESCALAB 250Xi spectrometer. The photocurrent response experiment was performed on a photoelectrochemical workstation (CIMPS-2, Zahner) with a three-electrode system; 300 W Xe lamp and Na_2SO_4 aqueous solution (0.1 M) were used as the light source and electrolyte solution, respectively. The hydroxyl radicals were detected using a fluorescence spectrophotometer (Hitachi F-7000).

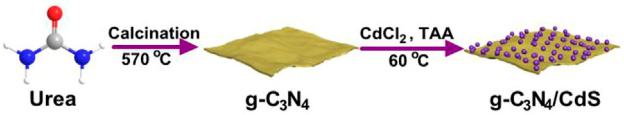

SCHEME 1 | Schematic representation of the synthesis processes of g-C_3N_4/CdS hybrids.

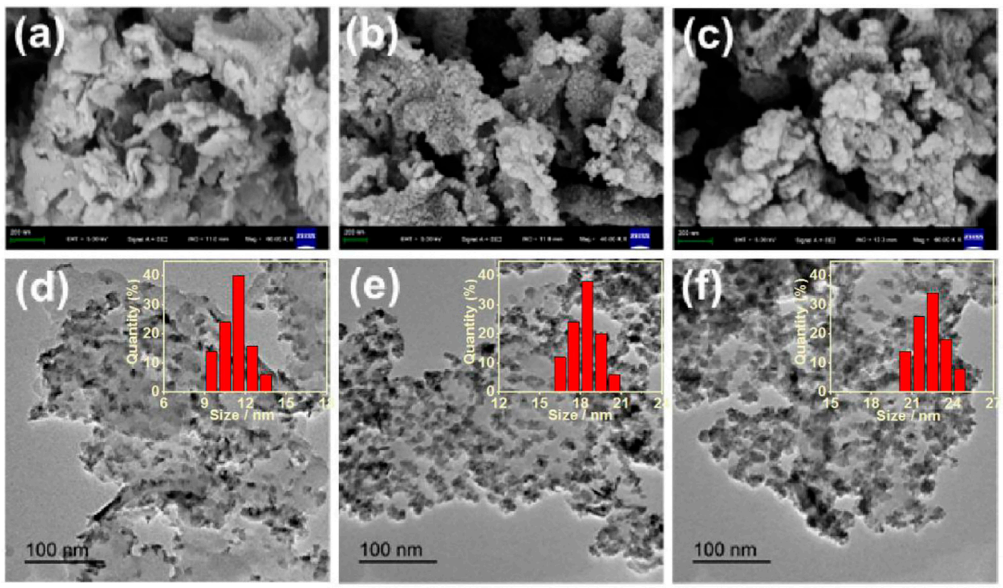

FIGURE 1 | (A–C) SEM and **(D–F)** TEM images of (a, d) g-C_3N_4/CdS-1 (b, e) g-C_3N_4/CdS-2, and (c, f) g-C_3N_4/CdS-3 hybrids. Inset: The statistical size distributions of CdS nanoparticles for g-C_3N_4/CdS-1/2/3 hybrids.

RESULTS AND DISCUSSIONS

Morphologies and Structural Characterization

The synthesis processes of g-C_3N_4/CdS hybrids are shown in **Scheme 1**. The morphology and structure of g-C_3N_4/CdS samples were characterized by SEM and TEM, as given in **Figure 1**. **Supplementary Figure S1** is the TEM image of the pure g-C_3N_4 sample with a layered structure, which can offer a substrate for the arching of CdS nanoparticles. For the g-C_3N_4/CdS samples (**Figure 1**), it should be noted that the CdS nanoparticles are well loaded onto the g-C_3N_4 nanosheets. The amount and particle sizes of CdS nanoparticles can be tuned by changing the amount of the $CdCl_2$ precursor. As demonstrated in **Figures 1A,D**, for the sample g-C_3N_4/CdS-1, CdS nanoparticles were evenly dispersed on g-C_3N_4 nanosheets with a size narrowed by about 11.5 nm. With increasing the amount of the $CdCl_2$ precursor, more nanoparticles with a larger size, up to 18.0 nm, can be observed for sample g-C_3N_4/CdS-2 (**Figures 1B,E**). When the amount of $CdCl_2$ was increased to 22.5 mg, for sample g-C_3N_4/CdS-3, the size distribution of CdS nanoparticles turns to be wider, and CdS nanoparticles with a diameter of ~23.5 and ~8.8 nm can be observed (**Figures 1C,F**). The statistical size distributions of CdS nanoparticles for g-C_3N_4/CdS-1/2/3 hybrids are also given in **Figure 1**.

As seen from **Figures 2A–C**, TEM, HRTEM, and EDX mapping indicated the successful loading of CdS nanoparticles on a g-C_3N_4 nanosheet. The TEM image (**Figure 2A**) shows a high distribution of CdS nanoparticles with average sizes of about ~18 nm dispersed on g-C_3N_4 nanosheets. The HRTEM image (**Figure 2B**) gives two sets of distinct lattice fringes, whereas the spacing of about 0.316 and 0.321 nm, corresponding to the (101) and (002) planes of CdS and g-C_3N_4, respectively (Wang et al., 2017a; Zhang et al., 2017; Chiu et al., 2019). Obviously, EDX mappings demonstrate the existence of C, N, Cd, and S (**Figures 2D–H**), suggesting the uniform distribution of Cd and S elements from g-C_3N_4/CdS (**Figure 2C**), confirming the good connection between CdS and g-C_3N_4.

The crystal phases of g-C_3N_4, CdS, and g-C_3N_4/CdS samples were analyzed by XRD. As shown in **Figure 3A**, all diffraction peaks for g-C_3N_4 and CdS can be observed. The two strong diffraction peaks clearly shown at 12.8° and 27.6° can be ascribed to (100) and (002) crystal planes of g-C_3N_4 (PDF#50-1,250), which can be associated with typical in-plane tri-s-triazine and graphitic stacking of g-C_3N_4 (Xu et al., 2020). Furthermore, diffraction peaks at 24.8°, 26.5°, and 28.3° are well matched

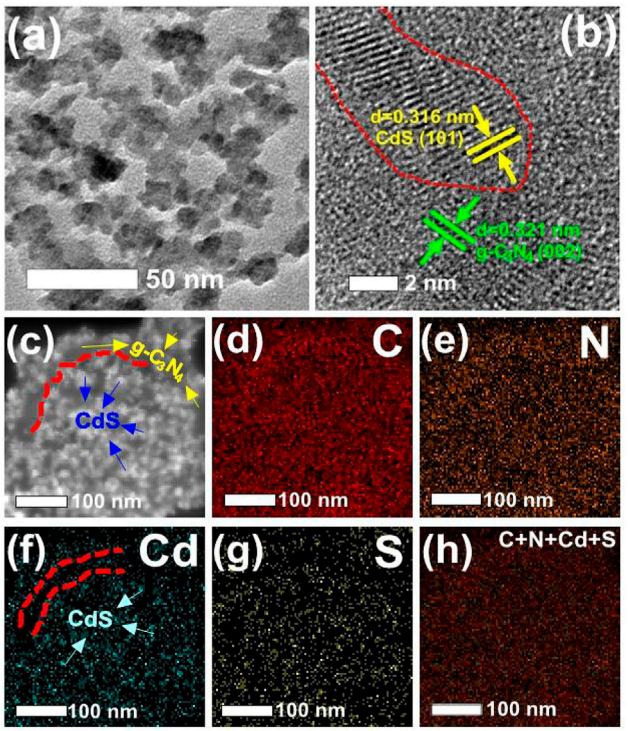

FIGURE 2 | (A) TEM, **(B)** HRTEM, and **(C)** HAADF-STEM images of g-C_3N_4/CdS-2 hybrids. **(D–G)** Elemental mappings of (d) C, (e) N, (f) Cd, (g) S, and (h) C + N + Cd + S of g-C_3N_4/CdS-2 hybrids.

for those of hexagonal CdS (PDF#41-1,049). The pore structures and specific surface areas for prepared samples were determined by BET measurements. The corresponding results of sample CdS nanoparticles, g-C_3N_4 nanosheets, and g-C_3N_4/CdS-(1-3) hybrids are given in **Figure 3B** and **Supplementary Figure S2**, suggesting the existence of mesoporous pores. The S_{BET} of sample g-C_3N_4/CdS-2 is the highest S_{BET} among all the prepared samples, which can provide more reactive sites and ensure better contact catalysts with reagents during the photocatalytic reactions. The light absorption of pristine g-C_3N_4, CdS nanoparticles, and the as-prepared g-C_3N_4/CdS samples are shown in **Figures 3C,D**. The absorption around 470 nm is assigned for pristine g-C_3N_4. It can be obviously observed that the absorption ranges of prepared g-C_3N_4/CdS samples were extended. The resulting values of E_g for CdS, g-C_3N_4, and g-C_3N_4/CdS-(1-3) samples were 2.16, 2.60, 2.11, 1.91, and 2.05 eV, respectively. The enhanced absorption for g-C_3N_4/CdS is probably due to the formation of heterojunctions. Sample g-C_3N_4/CdS-2 with appropriate CdS particle size has the lowest bandgap, the stronger background absorption could be ascribed to the synergistic interaction between g-C_3N_4 nanosheets and CdS nanoparticles, and the photoinduced electrons from the LUMO of CdS could adequately inject into the conduction band of g-C_3N_4, leading to the reduced initial bandgap values of CdS and g-C_3N_4, separately (Al Marzouqi et al., 2019).

The surface composition of the g-C_3N_4, CdS, and g-C_3N_4/CdS samples was studied by XPS analyses, as shown in **Figure 4**. The survey XPS spectra (**Figure 4A**) provide the C 1s and N 1s peaks for g-C_3N_4, as well as S 2p and Cd 3 days peak for CdS. As shown in **Figure 4B**, the C 1s peak for g-C_3N_4/CdS at 284.3 eV, which is assigned to sp^2 C-C bonds from graphitic carbon. The other two peaks at 286.2 and 288.1 eV are attributed to N-C=N and π-excitation, respectively (Gao et al., 2014; Liang et al., 2019; Xu et al., 2020), These peaks show a slight shift while compared with g-C_3N_4. In **Figure 4C**, the two peaks at 405.5 and 412.2 eV could be ascribed to Cd $3d_{5/2}$ and Cd $3d_{3/2}$, of CdS from g-C_3N_4/CdS. In addition, the peaks at 161.1 and 162.3 eV are associated with S $2p_{3/2}$ and S $2p_{1/2}$ of CdS, respectively (**Figure 4D**; Ren et al., 2019; Wang et al., 2019; Ai et al., 2020). These peaks show a slight shift while compared with pristine CdS or g-C_3N_4, which confirm the interaction between the heterojunctions.

Photocatalytic Performances and Mechanism Discussion

The photocatalytic activities of g-C_3N_4, CdS, and g-C_3N_4/CdS samples were first evaluated with degradation of organic pollution, as given in **Figure 5**. It can be seen from **Figures 5A,B** that coupling with CdS shows a significant effect on RhB degradation for g-C_3N_4/CdS. The photocatalytic activity shows a trend of initially increasing and then decreasing with the increasing of CdS contents. The degradation efficiency of RhB can reach up to 99% within 40 min for g-C_3N_4/CdS-2 hybrids, which is remarkably enhanced than that for individual g-C_3N_4 nanosheets and CdS nanoparticles. The photocatalytic rate constant for the prepared g-C_3N_4/CdS-2 is 0.0849 min^{-1}, about 5.5 times higher than that for g-C_3N_4. The photocatalytic results demonstrate that the anchoring of CdS nanoparticles onto g-C_3N_4 nanosheets can remarkably be conducive to photocatalytic performance. The enhanced activity for sample g-C_3N_4/CdS-2 can be attributed to well-contacted interfaces, effective charge separation, stronger light absorption, and a higher surface area. Furthermore, the TOC analyzer was measured to investigate the mineralization of RhB. The changed TOC values during the photocatalytic process were tested, as shown in **Supplementary Table S1** and **Supplementary Figure S3**. The decayed TOC values suggest that RhB was decomposed into inorganic small molecules. As for MB (**Figures 5C,D**) and phenol (**Figures 5E,F**) degradation, g-C_3N_4/CdS-2 sample also exhibits much higher activity than others, where 96% of MB and 95% of phenol are degraded within 40 and 50 min, respectively. The degradation rate constants *k* for MB and phenol of prepared samples follow the same order with RhB degradation (**Figure 6A**). Moreover, the g-C_3N_4/CdS-2 sample can be recycled for six cycles without obviously decayed activity, and no scattering of CdS particles was found, indicating their excellent recyclability and stability (**Figure 6B** and **Supplementary Figure S4**).

The photocatalytic hydrogen evolution of prepared samples was investigated under visible-light irradiation with triethanolamine as the sacrificial reagent. As shown in **Figures 7A,B**, within 4 h measurement, pure g-C_3N_4 shows poor catalytic

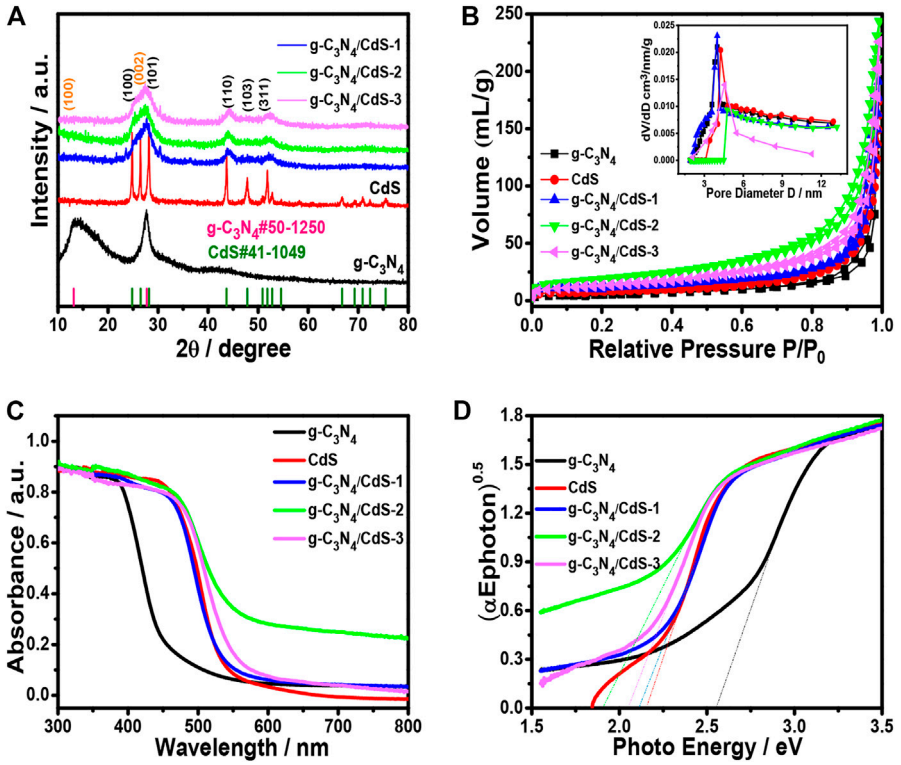

FIGURE 3 | (A) XRD patterns and **(B)** nitrogen adsorption–desorption isotherms of g-C_3N_4, CdS, and g-C_3N_4/CdS. Inset in **Figure 3B** is the corresponding BJH pore size distribution. **(C)** UV-Vis of absorption spectra and **(D)** the corresponding $(\alpha Ephoton)^{0.5}$ vs photon energy curves.

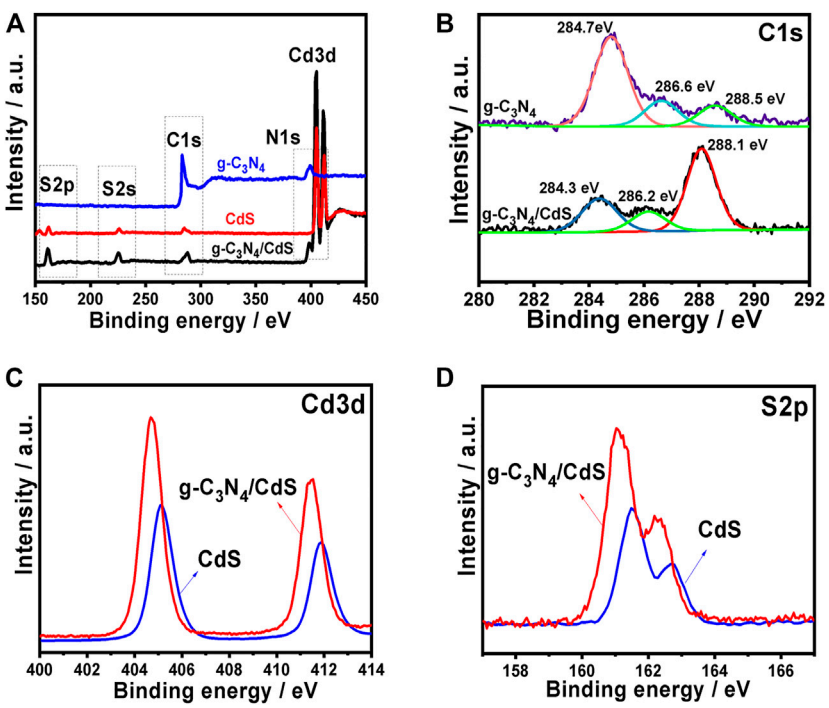

FIGURE 4 | Fully scanned XPS spectra of **(A)** g-C_3N_4, CdS, and g-C_3N_4/CdS; high-resolution XPS plots of **(B)** C 1 s, **(C)** Cd 3 days, and **(D)** S 2p.

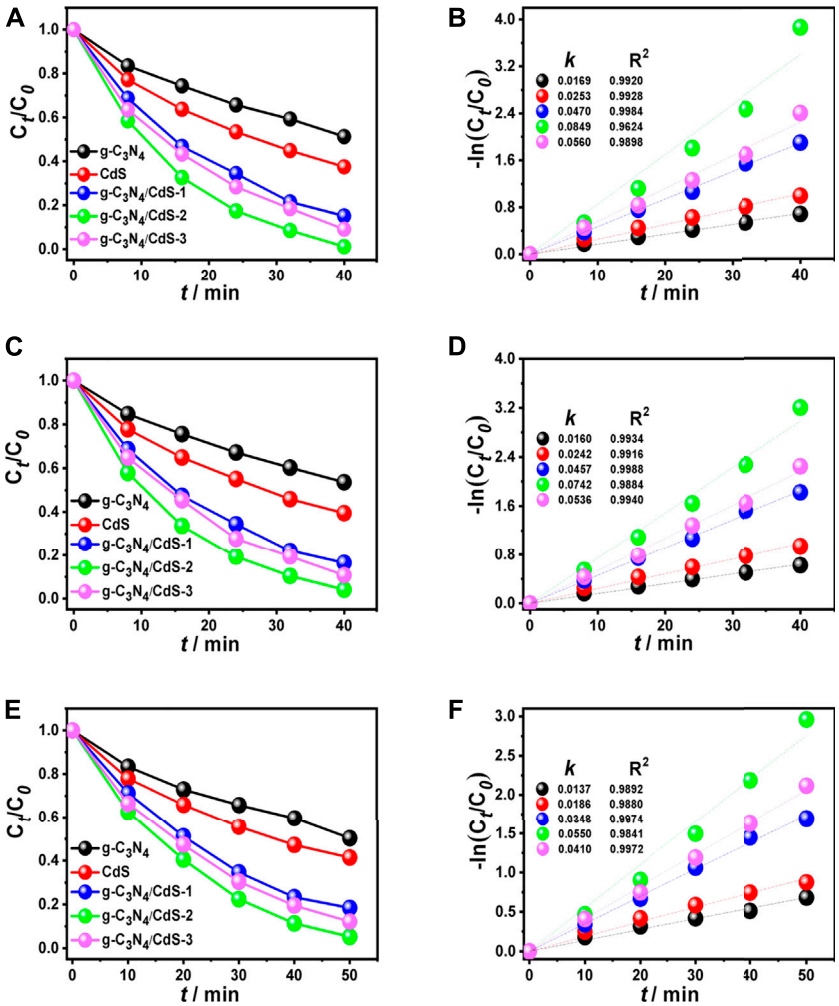

FIGURE 5 | Photocatalytic degradation under visible light irradiation of **(A)** RhB, **(C)** MB, and **(E)** phenol, and **(B,D,F)** corresponding apparent reaction rates using g-C_3N_4, CdS, and g-C_3N_4/CdS hybrids.

activity with the hydrogen generation rate of 237.8 μmol g^{-1} h^{-1}, and the hydrogen generation rate using g-C_3N_4 nanosheets is obviously improved after anchoring with CdS. The hydrogen evolution rate is increased first and then decayed with increasing CdS content, and the g-C_3N_4/CdS-2 sample exhibits the best hydrogen evolution rate (1,070.9 μmol g^{-1} h^{-1}), about 4 times as high as that for pure g-C_3N_4. The photocatalytic performance for g-C_3N_4/CdS-2 sample also surpasses the reported g-C_3N_4/CdS hybrids (**Supplementary Table S2**). In addition, the recyclability of photocatalytic hydrogen evolution was also measured, as shown in **Supplementary Figure S5a**. It can be seen that the hydrogen evolution performance of g-C_3N_4/CdS-2 shows no remarkable decline after 12 h, confirming its good stability.

As observed in **Figure 8A**, the photocurrent response of prepared samples is detected by photoelectrochemical testing to study the charge separation. It can be found that g-C_3N_4/CdS heterostructured samples show much higher photocurrent intensity than individual CdS and g-C_3N_4, which can possibly be ascribed to the heterostructure-induced acceleration of charge separation and transfer. (Tian et al., 2017; Ren et al., 2018; Zhu et al., 2019; Xu et al., 2019; Putri et al., 2020). In order to conduct an in-depth study on photocatalytic degradation, the scavenger test was performed using methanol as the scavenger. As shown in **Supplementary Figure S5b**, the photocatalytic performance of the RhB photodegradation rate is remarkably decreased after adding methanol, suggesting that the photogenerated holes play an important role in the photocatalytic process. In view of the results, a possible mechanism for g-C_3N_4/CdS sample with enhanced photocatalytic performance is put forward. The narrowed bandgap semiconductors g-C_3N_4 and CdS can be excited under light irradiation. Briefly, the electrons produced from g-C_3N_4 will transfer to CdS owing to the well-contacted interface, and the excited holes can move from CdS to the VB of g-C_3N_4. Consequently, the separation of photoinduced electrons and holes is effectively improved, and the lifetime of charges is improved (**Scheme 2**). The transferred strongly oxidizing holes on the VB of g-C_3N_4 can not only effectively inhibit photocorrosive damage to CdS during the reaction process but also directly degrade

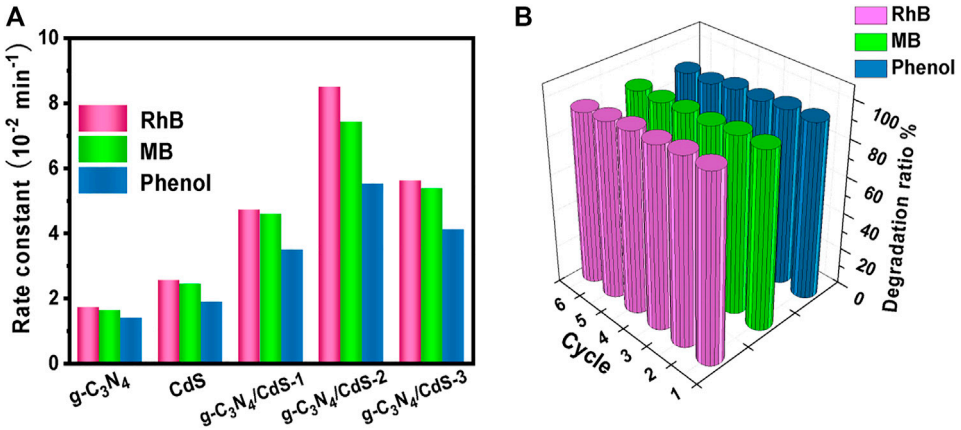

FIGURE 6 | (A) Comparison of rate constants of g-C_3N_4, CdS, and g-C_3N_4/CdS hybrids for organic pollution degradation (RhB, MB, and phenol) under visible light irradiation. **(B)** Recyclability measurements of RhB, MB, and phenol degradation under visible light irradiation by g-C_3N_4/CdS hybrids.

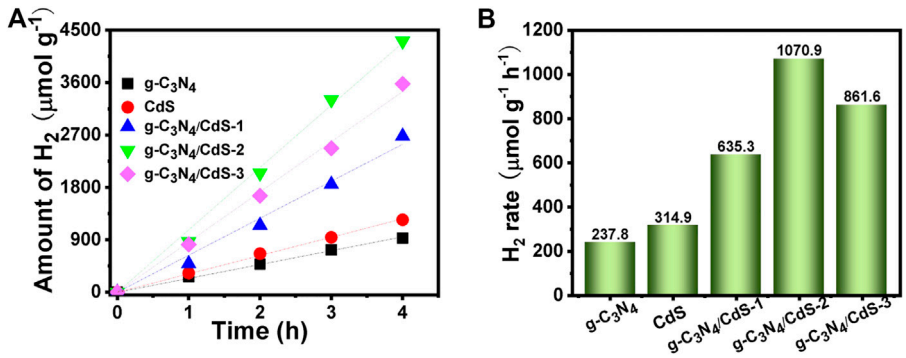

FIGURE 7 | (A,B) Photocatalytic hydrogen evolution on g-C_3N_4, CdS, and g-C_3N_4/CdS hybrids under visible light.

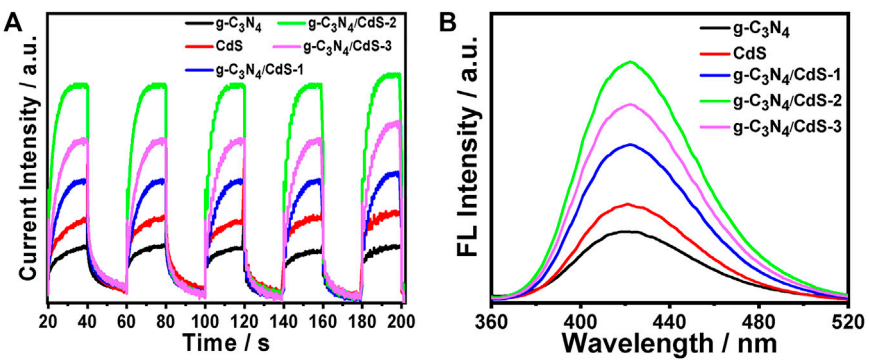

FIGURE 8 | (A) Photocurrents of g-C_3N_4, CdS, and g-C_3N_4/CdS hybrids under visible light irradiation under 0.8 V *versus* Ag/AgCl electrode bias. **(B)** Fluorescence spectra of g-C_3N_4, CdS, and g-C_3N_4/CdS hybrids in a basic solution of terephthalic acid under visible light irradiation at a fixed time.

the target molecules. In the process of photocatalytic reaction, the photoexcited electrons may reduce H^+ into hydrogen. Meanwhile, the accumulated electrons on the surface of CdS can oxidize the adsorbed dissolved O_2 to produce $\bullet O_2^-$ and subsequently form •OH. The formation of powerful reactive species ($\bullet O_2^-$ and •OH) can effectively degrade the organic pollutant molecules (Huo et al., 2012; Wu et al., 2018). The produced hydroxyl radicals can be measured by the fluorescence method with terephthalic acid as the probe reactant (Xiao et al., 2008; Yu et al., 2009; Wang et al., 2017b). The fluorescence spectra of all samples are shown in **Figure 8B**,

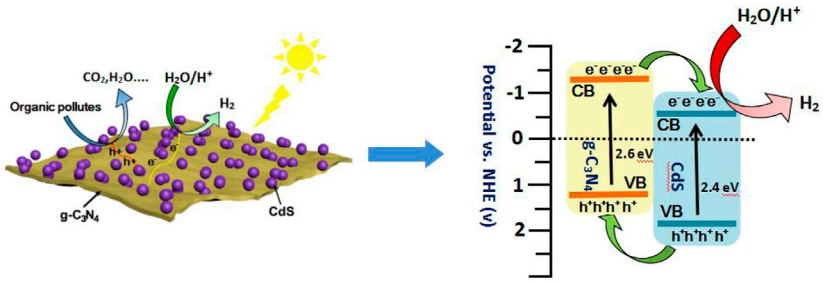

SCHEME 2 | Schematic illustration of band structure diagram and photoinduced carrier transfer of g-C_3N_4/CdS hybrids in the piezoelectric field under visible light irradiation.

where sample g-C_3N_4/CdS-2 can produce the largest amount of hydroxyl radicals. The obtained results are well consistent with those of the photocatalytic tests. The higher photocatalytic activity for g-C_3N_4/CdS sample can be ascribed to two main factors: 1) the significantly promoted charge separation by the constructed heterojunctions and 2) the higher specific surface area and excellent dispersion of prepared samples.

CONCLUSION

Heterostructured g-C_3N_4/CdS hybrids with controllable CdS nanoparticle anchoring on g-C_3N_4 nanosheets have been successfully prepared. The as-prepared samples show remarkably improved photocatalytic activity for organic pollute degradation and hydrogen generation under visible light. The experimental results demonstrate that the g-C_3N_4/CdS heterostructures exhibited superior photocatalytic hydrogen generation activity than individual g-C_3N_4 nanosheets and CdS nanoparticles, and the g-C_3N_4/CdS-2 sample has the highest visible light hydrogen generation rate as 1,070.9 μmol h^{-1} g^{-1}, which is 4 times higher than that for pure g-C_3N_4. The enhanced activity and stability are attributed to the intimated heterojunction between g-C_3N_4 nanosheets and CdS nanoparticles, which promotes interfacial charge separation and transportation. Finally, the well-dispersed CdS nanoparticles offer more reactive sites. The g-C_3N_4/CdS hybrids demonstrate high photocatalytic activity, stability, and recyclability, and hold great promise for practical application. This work could provide new perspective into the construction and manufacture of heterojunctions with highly efficient charge separation and migration for the solar energy conversion.

DATA AVAILABILITY STATEMENT

The original contributions presented in the study are included in the article/**Supplementary Material**; further inquiries can be directed to the corresponding authors.

AUTHOR CONTRIBUTIONS

MGW performed the main experiment. JH conceived and directed the project. MGW, MW, and FP analyzed all the data and drew the figures. MGW wrote the manuscript with the help of XHS and JH. All authors agreed to the published version of the manuscript.

FUNDING

The authors gratefully acknowledge financial support from the National Natural Science Foundation of China (21922202), the Natural Science Research Project of Jiangsu Higher Education Institutions (19KJB150043 and 18KJB430031), and Qing Lan Project of Jiangsu Higher Education Institutions. We would also like to acknowledge the technical support received at the Testing Center of Yangzhou University.

SUPPLEMENTARY MATERIAL

The Supplementary Material for this article can be found online at: https://www.frontiersin.org/articles/10.3389/fchem.2021.746031/full#supplementary-material

REFERENCES

Ai, Z., Zhang, K., Shi, D., Chang, B., Shao, Y., Zhang, L., et al. (2020). Band-matching Transformation between CdS and BCNNTs with Tunable P-N Homojunction for Enhanced Photocatalytic Pure Water Splitting. *Nano Energy* 69, 104408. doi:10.1016/j.nanoen.2019.104408

Al Marzouqi, F., Kim, Y., and Selvaraj, R. (2019). Shifting of the Band Edge and Investigation of Charge Carrier Pathways in the CdS/g-C3n4 Heterostructure for Enhanced Photocatalytic Degradation of Levofloxacin. *New J. Chem.* 43, 9784–9792. doi:10.1039/c9nj01782h

Bai, X., Wang, L., Zong, R., and Zhu, Y. (2013). Photocatalytic Activity Enhanced via G-C3n4 Nanoplates to Nanorods. *J. Phys. Chem. C.* 117, 9952–9961. doi:10.1021/jp402062d

Cao, R., Yang, H., Zhang, S., and Xu, X. (2019). Engineering of Z-Scheme 2D/3D Architectures with Ni(OH)2 on 3D Porous G-C3n4 for Efficiently Photocatalytic H2 Evolution. *Appl. Catal. B: Environ.* 258, 117997. doi:10.1016/j.apcatb.2019.117997

Chang, X., Wang, T., and Gong, J. (2016). CO2 Photo-Reduction: Insights into CO2 Activation and Reaction on Surfaces of Photocatalysts. *Energy Environ. Sci.* 9, 2177–2196. doi:10.1039/c6ee00383d

Chen, L., Xu, Y., and Chen, B. (2019). *In Situ* photochemical Fabrication of CdS/g-C3n4 Nanocomposites with High Performance for Hydrogen Evolution under Visible Light. *Appl. Catal. B: Environ.* 256, 117848. doi:10.1016/j.apcatb.2019.117848

Chen, X., Shen, S., Guo, L., and Mao, S. S. (2010). Semiconductor-based Photocatalytic Hydrogen Generation. *Chem. Rev.* 110, 6503–6570. doi:10.1021/cr1001645

Chiu, Y.-H., Naghadeh, S. B., Lindley, S. A., Lai, T.-H., Kuo, M.-Y., Chang, K.-D., et al. (2019). Yolk-shell Nanostructures as an Emerging Photocatalyst Paradigm for Solar Hydrogen Generation. *Nano Energy* 62, 289–298. doi:10.1016/j.nanoen.2019.05.008

Cui, Y. (2015). *In-situ* Synthesis of C3N4/CdS Composites with Enhanced Photocatalytic Properties. *Chin. J. Catal.* 36, 372–379. doi:10.1016/s1872-2067(14)60237-0In

Deng, P., Xiong, J., Lei, S., Wang, W., Ou, X., Xu, Y., et al. (2019). Nickel Formate Induced High-Level *In Situ* Ni-Doping of G-C3n4 for a Tunable Band Structure and Enhanced Photocatalytic Performance. *J. Mater. Chem. A.* 7, 22385–22397. doi:10.1039/c9ta04559g

Duan, L., Liu, H., Muhammad, Y., Shi, L., Wu, H., Zhang, J., et al. (2019). Photo-mediated Co-loading of Highly Dispersed MnOx-Pt on G-C3n4 Boosts the Ambient Catalytic Oxidation of Formaldehyde. *Nanoscale* 11, 8160–8169. doi:10.1039/c8nr08731h

Fan, G., Du, B., Zhou, J., Yu, W., Chen, Z., and Yang, S. (2020). Stable Ag2O/g-C3n4 P-N Heterojunction Photocatalysts for Efficient Inactivation of Harmful Algae under Visible Light. *Appl. Catal. B: Environ.* 265, 118610. doi:10.1016/j.apcatb.2020.118610

Fu, J., Chang, B., Tian, Y., Xi, F., and Dong, X. (2013). Novel C3N4-CdS Composite Photocatalysts with Organic-Inorganic Heterojunctions: *In Situ* Synthesis, Exceptional Activity, High Stability and Photocatalytic Mechanism. *J. Mater. Chem. A.* 1, 3083–3090. doi:10.1039/c2ta00672c

Fu, J., Xu, Q., Low, J., Jiang, C., and Yu, J. (2019). Ultrathin 2D/2D WO3/g-C3n4 Step-Scheme H2-Production Photocatalyst. *Appl. Catal. B: Environ.* 243, 556–565. doi:10.1016/j.apcatb.2018.11.011

Gao, D., Xu, Q., Zhang, J., Yang, Z., Si, M., Yan, Z., et al. (2014). Defect-related Ferromagnetism in Ultrathin Metal-free G-C3n4 Nanosheets. *Nanoscale* 6, 2577–2581. doi:10.1039/c3nr04743a

Guo, S., Tang, Y., Xie, Y., Tian, C., Feng, Q., Zhou, W., et al. (2017). P-doped Tubular G-C3n4 with Surface Carbon Defects: Universal Synthesis and Enhanced Visible-Light Photocatalytic Hydrogen Production. *Appl. Catal. B: Environ.* 218, 664–671. doi:10.1016/j.apcatb.2017.07.022

Han, C., Li, J., Ma, Z., Xie, H., Waterhouse, G. I. N., Ye, L., et al. (2018). Black Phosphorus Quantum Dot/g-C3n4 Composites for Enhanced CO2 Photoreduction to CO. *Sci. China Mater.* 61, 1159–1166. doi:10.1007/s40843-018-9245-y

Huo, Y., Zhang, J., Miao, M., and Jin, Y. (2012). Solvothermal Synthesis of Flower-like BiOBr Microspheres with Highly Visible-Light Photocatalytic Performances. *Appl. Catal. B: Environ.* 111-112, 334–341. doi:10.1016/j.apcatb.2011.10.016

Ji, C., Yin, S.-N., Sun, S., and Yang, S. (2018). An *In Situ* Mediator-free Route to Fabricate Cu2O/g-C3n4 Type-II Heterojunctions for Enhanced Visible-Light Photocatalytic H2 Generation. *Appl. Surf. Sci.* 434, 1224–1231. doi:10.1016/j.apsusc.2017.11.233

Li, W., Guo, Z., Jiang, L., Zhong, L., Li, G., Zhang, J., et al. (2020). Facile *In Situ* Reductive Synthesis of Both Nitrogen Deficient and Protonated G-C3n4 Nanosheets for the Synergistic Enhancement of Visible-Light H2 Evolution. *Chem. Sci.* 11, 2716–2728. doi:10.1039/c9sc05060d

Liang, M., Borjigin, T., Zhang, Y., Liu, B., Liu, H., and Guo, H. (2019). Controlled Assemble of Hollow Heterostructured G-C3N4@CeO2 with Rich Oxygen Vacancies for Enhanced Photocatalytic CO2 Reduction. *Appl. Catal. B: Environ.* 243, 566–575. doi:10.1016/j.apcatb.2018.11.010

Lin, B., Yang, G., Yang, B., and Zhao, Y. (2016). Construction of Novel Three Dimensionally Ordered Macroporous Carbon Nitride for Highly Efficient Photocatalytic Activity. *Appl. Catal. B: Environ.* 198, 276–285. doi:10.1016/j.apcatb.2016.05.069

Liu, C., Huang, H., Ye, L., Yu, S., Tian, N., Du, X., et al. (2017). Intermediate-mediated Strategy to Horn-like Hollow Mesoporous Ultrathin G-C3n4 Tube with Spatial Anisotropic Charge Separation for superior Photocatalytic H2 Evolution. *Nano Energy* 41, 738–748. doi:10.1016/j.nanoen.2017.10.031

Liu, J., Fang, W., Wei, Z., Qin, Z., Jiang, Z., and Shangguan, W. (2018). Efficient Photocatalytic Hydrogen Evolution on N-Deficient G-C3n4 Achieved by a Molten Salt post-treatment Approach. *Appl. Catal. B: Environ.* 238, 465–470. doi:10.1016/j.apcatb.2018.07.021

Liu, Y., Zhang, P., Tian, B., and Zhang, J. (2015). Core-Shell Structural CdS@SnO2 Nanorods with Excellent Visible-Light Photocatalytic Activity for the Selective Oxidation of Benzyl Alcohol to Benzaldehyde. *ACS Appl. Mater. Inter.* 7, 13849–13858. doi:10.1021/acsami.5b04128

Ng, S. F., Lau, M. Y. L., and Ong, W. J. (2021). Engineering Layered Double Hydroxide-Based Photocatalysts toward Artificial Photosynthesis: State-of-the-Art Progress and Prospects. *Sol. RRL* 5, 2000535. doi:10.1002/solr.202000535

Niu, P., Qiao, M., Li, Y., Huang, L., and Zhai, T. (2018). Distinctive Defects Engineering in Graphitic Carbon Nitride for Greatly Extended Visible Light Photocatalytic Hydrogen Evolution. *Nano Energy* 44, 73–81. doi:10.1016/j.nanoen.2017.11.059

Ong, W. J., Putri, L. K., and Mohamed, A. R. (2020). Rational Design of Carbon-Based 2D Nanostructures for Enhanced Photocatalytic CO 2 Reduction: A Dimensionality Perspective. *Chem. Eur. J.* 26, 9710–9748. doi:10.1002/chem.202000708

Putri, L. K., Ng, B.-J., Ong, W.-J., Lee, H. W., Chang, W. S., Mohamed, A. R., et al. (2020). Energy Level Tuning of CdSe Colloidal Quantum Dots in Ternary 0D-2D-2D CdSe QD/B-rGO/O-gC3N4 as Photocatalysts for Enhanced Hydrogen Generation. *Appl. Catal. B: Environ.* 265, 118592. doi:10.1016/j.apcatb.2020.118592

Qi, J., Zhang, W., and Cao, R. (2018). Solar-to-hydrogen Energy Conversion Based on Water Splitting. *Adv. Energ. Mater.* 8, 1701620. doi:10.1002/aenm.201701620

Ren, J.-T., Yuan, K., Wu, K., Zhou, L., and Zhang, Y.-W. (2019). A Robust CdS/In2O3 Hierarchical Heterostructure Derived from a Metal-Organic Framework for Efficient Visible-Light Photocatalytic Hydrogen Production. *Inorg. Chem. Front.* 6, 366–375. doi:10.1039/c8qi01202d

Ren, X., Gao, P., Kong, X., Jiang, R., Yang, P., Chen, Y., et al. (2018). NiO/Ni/TiO2 Nanocables with Schottky/p-N Heterojunctions and the Improved Photocatalytic Performance in Water Splitting under Visible Light. *J. Colloid Interf. Sci.* 530, 1–8. doi:10.1016/j.jcis.2018.06.071

Shi, L., Chang, K., Zhang, H., Hai, X., Yang, L., Wang, T., et al. (2016). Drastic Enhancement of Photocatalytic Activities over Phosphoric Acid Protonated Porous G-C3N4Nanosheets under Visible Light. *Small* 12, 4431–4439. doi:10.1002/smll.201601668

Shi, X., Fujitsuka, M., Lou, Z., Zhang, P., and Majima, T. (2017). *In Situ* nitrogen-doped Hollow-TiO2/g-C3n4 Composite Photocatalysts with Efficient Charge Separation Boosting Water Reduction under Visible Light. *J. Mater. Chem. A.* 5, 9671–9681. doi:10.1039/c7ta01888f

Sun, J., Zhang, J., Zhang, M., Antonietti, M., Fu, X., and Wang, X. (2012). Bioinspired Hollow Semiconductor Nanospheres as Photosynthetic Nanoparticles. *Nat. Commun.* 3, 1139. doi:10.1038/ncomms2152

Tahir, M., Cao, C., Mahmood, N., Butt, F. K., Mahmood, A., Idrees, F., et al. (2014). Multifunctional G-C3n4 Nanofibers: A Template-Free Fabrication and Enhanced Optical, Electrochemical, and Photocatalyst Properties. *ACS Appl. Mater. Inter.* 6, 1258–1265. doi:10.1021/am405076b

Teng, Z., Lv, H., Wang, C., Xue, H., Pang, H., and Wang, G. (2017). Bandgap Engineering of Ultrathin Graphene-like Carbon Nitride Nanosheets with Controllable Oxygenous Functionalization. *Carbon* 113, 63–75. doi:10.1016/j.carbon.2016.11.030

Tian, Q., Wu, W., Liu, J., Wu, Z., Yao, W., Ding, J., et al. (2017). Dimensional Heterostructures of 1D CdS/2D ZnIn2S4 Composited with 2D Graphene: Designed Synthesis and superior Photocatalytic Performance. *Dalton Trans.* 46, 2770–2777. doi:10.1039/c7dt00018a

Tong, H., Ouyang, S., Bi, Y., Umezawa, N., Oshikiri, M., and Ye, J. (2012). Nano-photocatalytic Materials: Possibilities and Challenges. *Adv. Mater.* 24, 229–251. doi:10.1002/adma.201102752

Vu, N.-N., Kaliaguine, S., and Do, T.-O. (2020). Synthesis of the G-C3N4/CdS Nanocomposite with a Chemically Bonded Interface for Enhanced Sunlight-Driven CO2 Photoreduction. *ACS Appl. Energ. Mater.* 3, 6422–6433. doi:10.1021/acsaem.0c00656

Wan, C., Zhou, L., Sun, L., Xu, L., Cheng, D.-g., Chen, F., et al. (2020). Boosting Visible-Light-Driven Hydrogen Evolution from Formic Acid over AgPd/2D G-C3n4 Nanosheets Mott-Schottky Photocatalyst. *Chem. Eng. J.* 396, 125229. doi:10.1016/j.cej.2020.125229

Wang, M., Han, J., Hu, Y., and GuoMesoporous, R. C. (2017). Mesoporous C, N-Codoped TiO2 Hybrid Shells with Enhanced Visible Light Photocatalytic Performance. *RSC Adv.* 7, 15513–15520. doi:10.1039/c7ra00985b

Wang, P., Wu, T., Wang, C., Hou, J., Qian, J., and Ao, Y. (2017). Combining Heterojunction Engineering with Surface Cocatalyst Modification to Synergistically Enhance the Photocatalytic Hydrogen Evolution Performance of Cadmium Sulfide Nanorods. *ACS Sustain. Chem. Eng.* 5, 7670–7677. doi:10.1021/acssuschemeng.7b01043

Wang, S., Zhu, B., Liu, M., Zhang, L., Yu, J., and Zhou, M. (2019). Direct Z-Scheme ZnO/CdS Hierarchical Photocatalyst for Enhanced Photocatalytic H2-Production Activity. *Appl. Catal. B: Environ.* 243, 19–26. doi:10.1016/j.apcatb.2018.10.019

Wu, Y., Wang, H., Tu, W., Wu, S., Liu, Y., Tan, Y. Z., et al. (2018). Petal-like CdS Nanostructures Coated with Exfoliated Sulfur-Doped Carbon Nitride via Chemically Activated Chain Termination for Enhanced Visible-Light-Driven Photocatalytic Water Purification and H2 Generation. *Appl. Catal. B: Environ.* 229, 181–191. doi:10.1016/j.apcatb.2018.02.029

Xiao, Q., Si, Z., Zhang, J., Xiao, C., and Tan, X. (2008). Photoinduced Hydroxyl Radical and Photocatalytic Activity of Samarium-Doped TiO2 Nanocrystalline. *J. Hazard. Mater.* 150, 62–67. doi:10.1016/j.jhazmat.2007.04.045

Xu, F., Mo, Z., Yan, J., Fu, J., Song, Y., El-Alami, W., et al. (2020). Nitrogen-rich Graphitic Carbon Nitride Nanotubes for Photocatalytic Hydrogen Evolution with Simultaneous Contaminant Degradation. *J. Colloid Interf. Sci.* 560, 555–564. doi:10.1016/j.jcis.2019.10.089

Xu, H., Wang, Y., Dong, X., Zheng, N., Ma, H., and Zhang, X. (2019). Fabrication of In2O3/In2S3 Microsphere Heterostructures for Efficient and Stable Photocatalytic Nitrogen Fixation. *Appl. Catal. B: Environ.* 257, 117932. doi:10.1016/j.apcatb.2019.117932

Yang, F., Liu, D., Li, Y., Cheng, L., and Ye, J. (2019). Salt-template-assisted Construction of Honeycomb-like Structured G-C3n4 with Tunable Band Structure for Enhanced Photocatalytic H2 Production. *Appl. Catal. B: Environ.* 240, 64–71. doi:10.1016/j.apcatb.2018.08.072

Yu, H., Shi, R., Zhao, Y., Bian, T., Zhao, Y., Zhou, C., et al. (2017). Alkali-assisted Synthesis of Nitrogen Deficient Graphitic Carbon Nitride with Tunable Band Structures for Efficient Visible-Light-Driven Hydrogen Evolution. *Adv. Mater.* 29, 1605148. doi:10.1002/adma.201605148

Yu, J., Wang, W., Cheng, B., and Su, B.-L. (2009). Enhancement of Photocatalytic Activity of Mesporous TiO2 Powders by Hydrothermal Surface Fluorination Treatment. *J. Phys. Chem. C.* 113, 6743–6750. doi:10.1021/jp900136q

Yu, X., Ng, S. F., Putri, L. K., Tan, L. L., Mohamed, A. R., and Ong, W. J. (2021). Point-Defect Engineering: Leveraging Imperfections in Graphitic Carbon Nitride (g-C 3 N 4) Photocatalysts toward Artificial Photosynthesis. *Small*, 2006851. doi:10.1002/smll.202006851

Zhang, G., Lan, Z.-A., Lin, L., Lin, S., and Wang, X. (2016). Overall Water Splitting by Pt/g-C3N4photocatalysts without Using Sacrificial Agents. *Chem. Sci.* 7, 3062–3066. doi:10.1039/c5sc04572j

Zhang, J., Wang, Y., Jin, J., Zhang, J., Lin, Z., Huang, F., et al. (2013). Efficient Visible-Light Photocatalytic Hydrogen Evolution and Enhanced Photostability of Core/Shell CdS/g-C3n4 Nanowires. *ACS Appl. Mater. Inter.* 5, 10317–10324. doi:10.1021/am403327g

Zhang, P., Liu, Y., Tian, B., Luo, Y., and Zhang, J. (2017). Synthesis of Core-Shell Structured CdS@CeO 2 and CdS@TiO 2 Composites and Comparison of Their Photocatalytic Activities for the Selective Oxidation of Benzyl Alcohol to Benzaldehyde. *Catal. Today* 281, 181–188. doi:10.1016/j.cattod.2016.05.042

Zhou, C., Shi, R., Shang, L., Wu, L.-Z., Tung, C.-H., and Zhang, T. (2018). Template-free Large-Scale Synthesis of G-C3n4 Microtubes for Enhanced Visible Light-Driven Photocatalytic H2 Production. *Nano Res.* 11, 3462–3468. doi:10.1007/s12274-018-2003-2

Zhu, Q., Qiu, B., Duan, H., Gong, Y., Qin, Z., Shen, B., et al. (2019). Electron Directed Migration Cooperated with Thermodynamic Regulation over Bimetallic NiFeP/g-C3n4 for Enhanced Photocatalytic Hydrogen Evolution. *Appl. Catal. B: Environ.* 259, 118078. doi:10.1016/j.apcatb.2019.118078

Conflict of Interest: The authors declare that the research was conducted in the absence of any commercial or financial relationships that could be construed as a potential conflict of interest.

Publisher's Note: All claims expressed in this article are solely those of the authors and do not necessarily represent those of their affiliated organizations, or those of the publisher, the editors, and the reviewers. Any product that may be evaluated in this article, or claim that may be made by its manufacturer, is not guaranteed or endorsed by the publisher.